NANO LETTERS

pubs.acs.org/NanoLett Letter

Electron Microscopy Probing Electron-Photon Interactions in SiC Nanowires with Ultrawide Energy and Momentum Match

Jinlong Du,[▽] Jin-hui Chen,[▽] Yuehui Li,[▽] Ruochen Shi, Mei Wu, Yun-Feng Xiao,* and Peng Gao*

Cite This: *Nano Lett.* 2022, 22, 6207−6214 Read Online

ACCESS | Metrics & More | Article Recommendations | Supporting Information

ABSTRACT: Light−matter interactions are commonly probed by optical spectroscopy, which, however, has some fundamental limitations such as diffraction-limited spatial resolution, tiny momentum transfer, and noncontinuous excitation/detection. In this work, through the use of scanning transmission electron microscopy−electron energy loss spectroscopy (STEM-EELS) with ultrawide energy and momentum match and subnanometer spatial resolution, the longitudinal Fabry−Perot (FP) resonating modes and the transverse whispering-gallery modes (WGMs) in individual SiC nanowires are simultaneously excited and detected, which span from near-infrared (∼1.2 μm) to ultraviolet (∼0.2 μm) spectral regime, and the momentum transfer can range up to 10^8 cm^{-1}. The size effects on the resonant spectra of nanowires are also revealed. This work provides an alternative technique to optical resonating spectroscopy and light−matter interactions in dielectric nanostructures, which is promising for modulating free electrons via photonic structures.

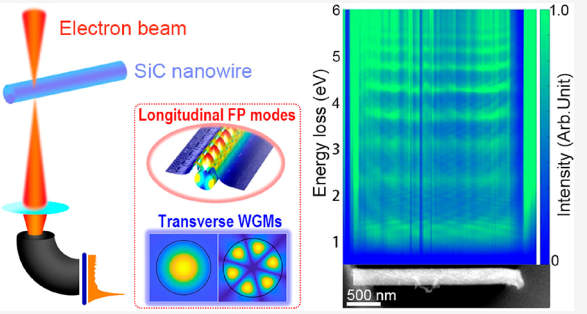

KEYWORDS: *EELS, STEM, SiC nanowire, optical resonance, electron-photon interaction*

Downloaded via PEKING UNIV on September 4, 2023 at 15:48:23 (UTC).
See https://pubs.acs.org/sharingguidelines for options on how to legitimately share published articles.

Nanophotonics, which focuses on the behavior of light on the nanoscale and the interaction of light with nanomaterials, helps reduce the size of various detectors and photonic devices, as small detectors tend to have a variety of desirable properties, including low noise, high speed, low power, etc. An important direction of nanophotonics is to trap light with nanomaterials.[1,2] The trapped light enabling subwavelength optics beyond the diffraction limit can enhance the light−matter interactions and thus find significant applications in subdiffraction imaging, nanoscale lasing, sensing, and surface-enhanced spectroscopy.[1−4] Understanding the light−matter interactions on the nanoscale is always a prerequisite for such photonic device design and applications. The laser-based optical spectroscopies such as absorption/scattering spectroscopy and photoluminescence spectroscopy have proved to be sophisticated tools for probing the photonic response of nanomaterials and nanostructures. For example, optical near-field techniques are widely used to image the evanescent field of nanostructures in the most advanced setups.[5,6] However, there are also a few limitations for conventional optical spectroscopy. First, due to the tiny momentum for photons, only those interactions with a small momentum transfer can be excited.[7−12] Second, some frequency windows (e.g., far-infrared) are not covered by the current commercial laser instruments.[13−16] Moreover, optical near-field techniques need to launch continuous-wave laser light spanning ultrawide frequency spectra to excite different-order waveguide modes, making not only the experimental study technically challenging but also the study of different waveguide mode couplings difficult.[13−16] Third, the spatial resolution of optical spectroscopy is constrained by the classical diffraction effects.[17−19] The interaction cross-sections between light and matter are typically small, thus it is usually difficult to probe the signal from the tiny nanostructures due to the limited spatial resolution and/or small cross-sections.[1,20,21] Therefore, it is highly desirable to overcome these limitations and to probe the fundamental interactions in tiny photonic nanostructures more efficiently.

Compared to the photons in optical techniques, the transferred momentum of electrons can be much larger when the injected electrons interact with matter.[8,22,23] The transferred momentum of a high energy electron beam scattered at angle (θ) is several orders of magnitude larger than that of a laser beam, which can be calculated by $\hbar\Delta k = \hbar k \sin\theta \cong \hbar k\theta$. For example, an electron beam with a collection semiangle of 25 mrad with a wavelength λ_e = 0.048 Å (60 keV) can give a transferred momentum Δk up to 3.0×10^8 cm^{-1}. In contrast, a laser beam with a divergence of 25 mrad at wavelength 600 nm gives a Δk of about 2.6×10^3 cm^{-1}. In addition, the range of transferred energy ΔE of the electrons is up to a kilo-electronvolt level, which is much larger than that in a laser beam.

Received: April 26, 2022
Revised: July 26, 2022
Published: July 29, 2022

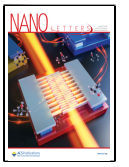

© 2022 American Chemical Society

https://doi.org/10.1021/acs.nanolett.2c01672
Nano Lett. 2022, 22, 6207−6214

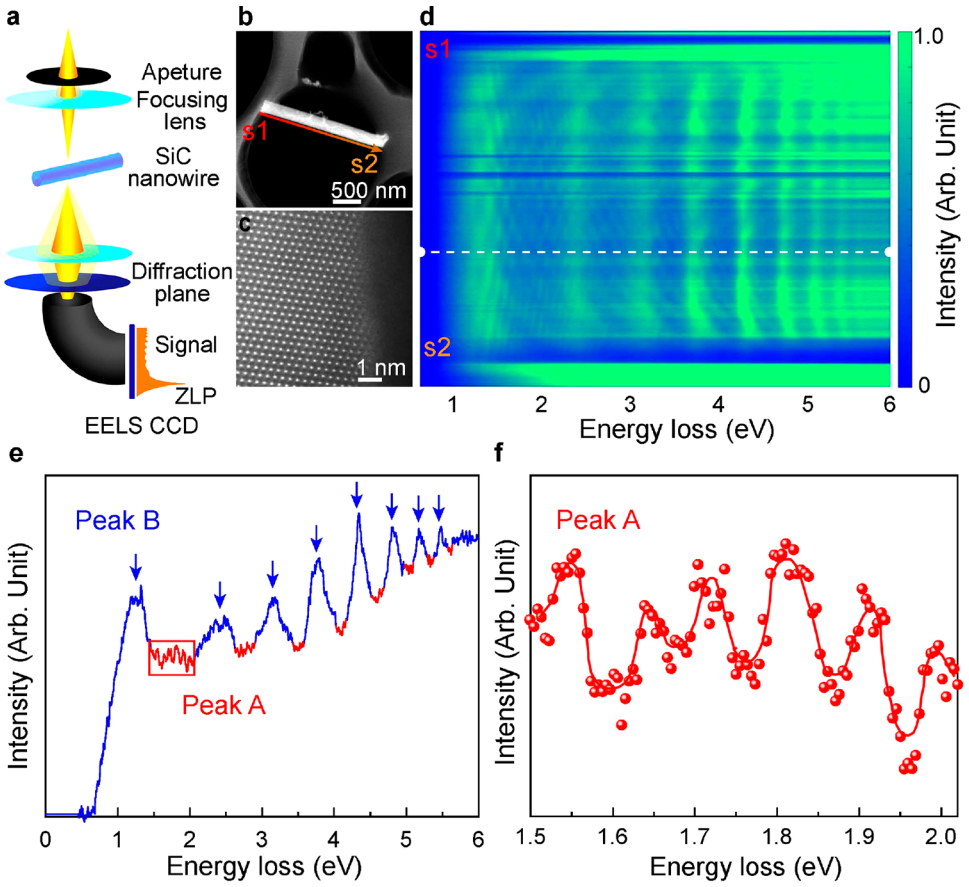

Figure 1. STEM-EELS measurements of 3C-SiC nanowires. (a) Schematic diagram of STEM-EELS system. (b) HAADF-STEM micrograph of a SiC nanowire with a diameter of ∼246 nm and length to diameter ratio of ∼9.8. (c) An atomic resolution HAADF-STEM image of the edge of the SiC nanowire viewed along the [110] direction. (d) Experimental EELS mapping of the nanowire, taken by an aloof electron beam scanning along the nanowire from s1 to s2. (e) EELS intensity line profile showing two types of peaks. (f) Enlarged view of the red box in e, showing the profile of peaks A.

The electron energy loss spectroscopy (EELS) incorporated in a scanning transmission electron microscope (i.e., STEM-EELS) equipped with an aberration corrector and monochromator offers considerable energy resolution and very high spatial resolution. The recent advances of monochromators in STEM enable an atom-wide kilo-electronvolt electron probe with about sub-10 meV energy resolution,[24−30] allowing atomically resolved EELS analysis of many physical excitations such as vibrational spectroscopy, phonon polaritons, and plasmons in an extremely wide continuous spectral range with subnanometer spatial resolution.[1,13,31−37] In addition, the high energy electrons can usually excite more multipole modes, even including the optical inactive dark modes.[9,38] However, research on the optical resonating spectroscopy of dielectric nanostructures via STEM-EELS has been rarely reported, which is mainly due to the optical frequency windows of the resonating modes usually overlap with plasmon/interband transitions of dielectric materials in EELS. In fact, for the dielectric microcavities with suitable dimensions (few tens of nanometers to micrometers), the intrinsically optical resonating spectra can be obtained without the influence of plasmon and interband transitions via aloof geometries (the electron beam positioned in the vacuum near the sample).[27,39,40]

In this work, we characterize the interactions of fast electrons and optical resonating modes in individual silicon carbide (SiC) nanowires with different diameters using STEM-EELS in the aloof mode where the electron beam is positioned several nanometers away from the sample. As a natural wide-bandgap material, SiC has important applications both in electronics and photonics. In particular, SiC photonics has emerged recently for the high refractive index and wide transparent windows (0.37−5.6 μm), which can avoid multiple photon absorption that bothers the Si photonics.[41,42] The longitudinal Fabry−Perot (FP) resonating modes and the transverse whispering-gallery modes (WGMs) of SiC nanowires are simultaneously excited and detected and span from near-infrared (∼1.2 μm) to ultraviolet (∼0.2 μm) and are much wider than that of conventional optical spectroscopy. The detected momentum transfer can be up to 10^8 cm^{-1}, which is also a few orders of magnitude larger than that of conventional optical spectroscopy. We systematically study many nanostructures to extract the size effect and reveal the underlying mechanism from both the analytical and numerical simulations. Moreover, the nanoscale decay length of resonant EELS is demonstrated to benefit from the subnanometer spatial resolution of STEM-EELS, which is contributed by the strongly localized electron−photon interactions in the SiC nanowire. This work provides the potential to investigate the resonant spectral properties on the nanoscale via STEM-EELS in an ultrawide energy and momentum range.

Figure 1a shows a schematic of STEM-EELS operation. The 60 kV focused electron beam with a 20 mrad convergence semiangle is positioned ∼10 nm away from the SiC nanowire, and the EELS data are collected with a 25 mrad collection semiangle. Figure 1b shows a low-magnification high-angle

https://doi.org/10.1021/acs.nanolett.2c01672
Nano Lett. 2022, 22, 6207−6214

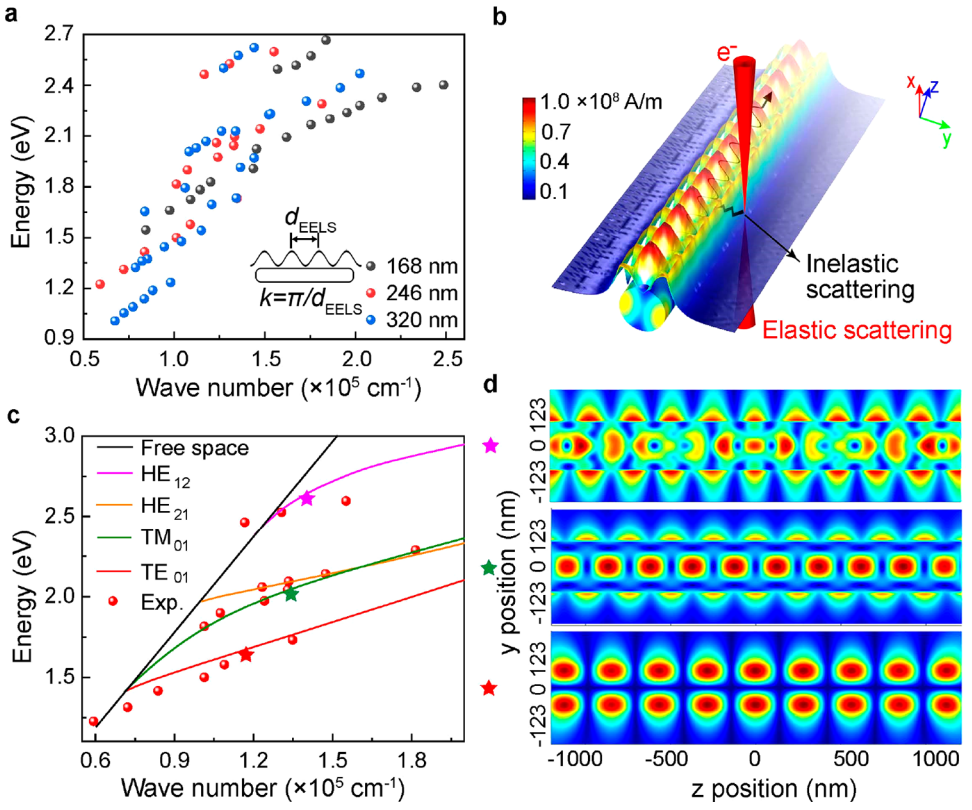

Figure 2. Size effects on the excitation of resonant waveguide modes of SiC nanowires. (a) The dispersion of peaks A in the SiC nanowire with different diameters. (b) Schematic diagram showing the excitation and measurement of FP resonating modes in SiC nanowires. (c) The measured (red dot) and calculated (line) dispersion of peaks A in the SiC nanowire with a diameter of ∼246 nm. The peaks A are induced by different photonic modes, i.e., TE_{01}, TM_{01}, $HE_{21,}$ and HE_{12}. (d) Calculated longitudinal propagating of TE_{01}, TM_{01}, and HE_{12} modes with $k = 1.12 \times 10^5$ cm^{-1}, $E = 1.55$ eV; $k = 1.27 \times 10^5$ cm^{-1}, $E = 1.99$ eV; and $k = 1.30 \times 10^5$ cm^{-1}, $E = 2.65$ eV, respectively, which are labeled by stars with different colors in c.

annular dark-field STEM (HAADF-STEM) micrograph of a single SiC nanowire. The diameter of the nanowire is ∼246 nm with a finite length (length to diameter ratio is ∼9.8). No porosities or dislocations are observed in the nanowire. The electron diffraction pattern along the [110] direction of the nanowire reveals the single crystal structure without any grain boundaries (see Figure S1a). Figure 1c shows an atomic-resolution HAADF-STEM image of the nanowire. On the basis of the electron diffraction pattern and the atomic image, the crystal structure of the SiC nanowire is confirmed to be 3C-SiC (Figure S1b). The two-dimensional space-EELS map of a SiC nanowire is shown in Figure 1d, which is acquired with the electron beam located at different positions in the aloof mode by scanning from s1 to s2 along the nanowire. The spectral intensity distribution along this line clearly shows an interference fringe. Unfolding the EELS spectra at a fixed position near the SiC nanowire, two groups of resonating peaks, i.e., peaks A and B, are resolved as shown in Figure 1e. The peaks that have significantly stronger intensity and larger peak energy intervals are regarded as peaks B, while the dense fringes with weaker modulated intensity and smaller peak energy intervals are peaks A. Peaks A are stacked with peaks B and can be more clearly observed in peaks B's valley regions, which are highlighted by red lines, and one is enlarged as shown in Figure 1f. In addition, no obvious intensity decreases of peaks A from the SiC nanowire tips to middle positions is observed, which is also verified in another nanowire with a larger length to diameter ratio of ∼22.5 (see Figure S2). The energies of peaks B do not change with a beam shift along the SiC nanowire. The energy intervals of peaks B decrease with the increase of energy and more than nine peaks B can be distinguished at an energy of 0−6 eV in this SiC nanowire.

To decipher the origin of peaks A, we convert the spatial field modulation of peaks A to the momentum space, i.e., $k = \pi/d_{EELS}$, where d_{EELS} is the distance of the spatial interference fringe, as shown in the inset of Figure 2a and Figure S3. Without a loss of generality, the dispersion relationships in the SiC nanowire with different diameters can be extracted from the experimental two-dimensional EELS map, as shown in Figure 2a. The dispersion curves show that the resonating energy increases with an increase of k. From the numerical calculations using COMSOL Multiphysics, it is found that peaks A of the EELS can be attributed to the longitudinal waveguide modes, which form FP resonance through the endface reflecting feedbacks. The dielectric dispersion of 3C-SiC is based on previous studies.[43] A detailed description of the analytical model can be seen in the Methods. Figure 2b shows the schematic of the excitation and measurement of FP resonating modes in SiC nanowires by electron beams. Free electrons pass near the SiC nanowire and interact with optical excitations. The nanowire plays as an optical cavity and increases the evanescent tails in a vacuum that interact with electrons.[36] Inelastic scattering of electrons and optical excitations of SiC nanowires naturally cause changes to the free-electron state, leading to the measured axial resonance spectroscopy. The calculated dispersion relationships of four different transverse electric (TE), transverse magnetic (TM), and hybrid electric (HE) waveguide modes, in a SiC nanowire with a diameter of 246 nm, are plotted in Figure 2c, i.e., TE_{01},

https://doi.org/10.1021/acs.nanolett.2c01672
Nano Lett. 2022, 22, 6207−6214

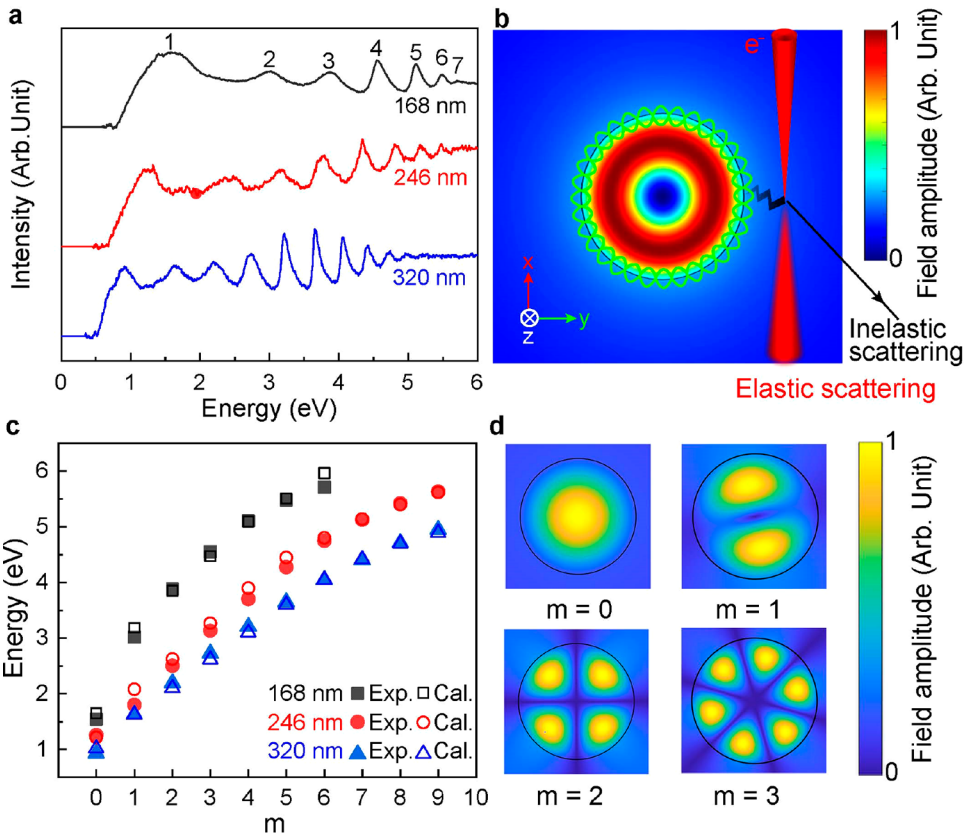

Figure 3. Size effects on the excitation of transverse whispering gallery mode (WGM) of the SiC nanowire. (a) Typical background-subtracted EELS profiles of SiC nanowires with different diameters. (b) Schematic showing interaction of free electrons with the excitation of WGM. (c) Experimental (solid dots) and calculated (hollow dots) energies of peaks B on SiC nanowires of different diameters. (d) The simulated two-dimensional cross-sectional field distribution of the first four whispering-gallery modes (mode order $m = 0-3$) with transverse magnetic polarization in a nanowire with a diameter of 320 nm.

TM_{01}, HE_{21}, and HE_{12}, in which the subscripts are used to complete the description of the waveguide modes. The typical field interference pattern of the TE_{01}, TM_{01}, and HE_{12} modes can be found in Figure 2d. The calculated dispersion relationships agree reasonably well with the experimental results, confirming that peaks A result from the longitudinal propagating of different waveguide modes with FP resonating effects. Note that the size effects on the excitation of resonant waveguide modes are also investigated, and it is shown that the energy of the first detected dispersion line decreases with the increase of nanowire diameter (Figure 2a), which agrees with the evanescent field properties of waveguide modes in nanowires. Additionally, it should be pointed out that in the low energy range close to the SiC optical phonon frequency, the dielectric constant of the nanowire dramatically changes, thus strong interactions between electrons and phonons lead to the emergence of the surface phonon polaritons. A previous study[31] shows that the surface phonon polaritons of SiC nanowires exist in the Reststrahlen band between ~99 meV and ~121 meV with strong size and geometry effects.

The features and origin of peaks B are discussed in Figure 3. Figure 3a shows the typical background-subtracted EELS profiles of SiC nanowires with different diameters. Since the energy of peaks B does not depend on the axial position of the SiC nanowires, we superimposed the EELS profiles in the axial direction and normalized the intensity to reduce the errors of the peak positions. It shows that the energy intervals of the peaks decrease with the increase of nanowire diameter, and the measurable peak numbers increase accordingly. Combined with the numerical calculation, we found that peaks B originate from the excitation of the transverse WGMs. Figure 3b shows the schematic of free electrons interacting with nanowires by the excitation of WGM. The SiC nanowire plays as a cylindrical cavity, and the WGMs with different orders can be efficiently excited due to the large momentum and energy transfer in the interaction of fast electrons and photonic resonant fields. Due to the high quality factor nature of WGMs compared with the FP modes, the spectral intensities of peaks B are significantly larger than those of peaks A. The measured resonating EELS energy can be corresponding to different orders of WGMs. Figure 3c shows the dependence of the experimental (solid dots) and calculated (hollow) energies of peaks B to the WGMs on SiC nanowires of different diameters. The simulated results agree well with experimental measurements. The features of these eigenmodes with different orders, i.e., m = 0, 1, 2, and 3, are plotted by cross-sectional field distribution, as shown in Figure 3d. The simultaneous detection of these high order cavity modes essentially originates from the wide momentum and energy match in electron−matter interactions. It should be noted that the resonating energy interval of WGMs is considerably reduced in the high-energy range, which leads to the accidental energy overlaps with the FP modes, as shown in Figure 1d. However, it is unlikely that they can form hybrid modes due to the radically different field profiles and propagation momenta between WGM and FP modes.

https://doi.org/10.1021/acs.nanolett.2c01672
Nano Lett. 2022, 22, 6207−6214

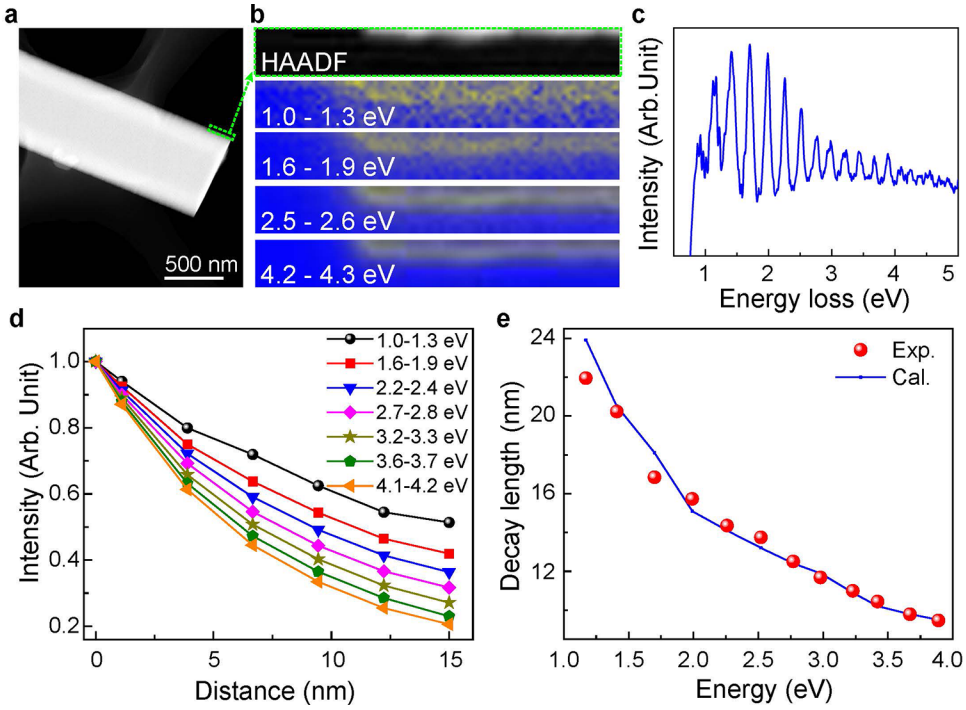

Figure 4. Spatial characterizations of EELS spectra for peaks B. (a) HAADF-STEM image of a SiC nanowire with a diameter of ~739 nm. (b) Experimental EELS maps near the surface of a SiC nanowire showing the spatial distribution of peaks B of various energies. (c) The background-subtracted EELS profiles of the SiC nanowire, showing the peaks supported from different orders of WGMs. (d) Normalized intensity profile showing the decay features of peaks B along the radial direction of SiC nanowires. (e) The experimental and calculated decay lengths of peaks B.

Compared with optical methods, STEM can easily achieve ultrahigh spatial resolution, so we are able to probe the spatial distribution of different WGMs. A SiC nanowire with diameter of ~739 nm (Figure 4a) is selected, and STEM-EELS measurements are performed near its surface, as shown in the green box in Figure 4a. The EELS signal of each spatial location and the corresponding HAADF image are recorded at the same time during scanning in real space. The electron beam size of STEM-EELS in this work is sub-nanometer, and the data were acquired by scanning in space near the SiC nanowire under aloof mode with ~2.5 nm for each scanning step (determined by scanning control and can achieve up to sub-nanometer if needed). The enlarged STEM image in Figure 4b and the corresponding EELS with different peaks (Figure 4c) near the surface of SiC nanowires show the spatial distribution of peaks B. We find that the intensities of peaks B decrease with the increase of distance to the SiC nanowire, and the higher energy modes decrease more quickly. Quantitatively, Figure 4d plots the EELS profiles along the radial direction of a SiC nanowire for different WGMs. The EELS intensity profiles of these WGMs are in accordance with exponential function $I_m = \exp(-d/\lambda_m)$, where I_m is the normalized intensity of EELS peaks B at distance d and λ_m is the decay length describing the distance from the edge to the position where the field decreases by a factor of $1/e$. The decay length of these EELS peaks B is plotted in Figure 4e. It shows that the decay length decreases with the increase of energy, i.e., the higher order the WGMs, the smaller the decay length of EELS profiles. Theoretically, the EELS profiles are determined by the correlation of the WGM field and the electron dipole radiation[44] (see Methods). Our numerical calculation is well consistent with the experimental results.

The transverse WGM and longitudinal FP resonance are two typical resonant modes in nanowire structures, which have been widely implemented in microlasers, sensors, and nonlinear optics.[45,46] For example, the WGM-based resonators were reported to be used in biomedical fields such as cancer detection.[47] The FP-based nanowire laser is a promising candidate for use in the next generation of optoelectronic devices.[46] This work implements STEM-EELS to simultaneously measure both transverse WGM and longitudinal FP modes for individual SiC nanowires and demonstrates the advantages of large momentum transfer, large energy range, and high spatial resolution for the resonant EELS, which are fully complementary to traditional optical methods. Note that many details of the optical cavity resonating modes (e.g., the fine features of FP mode with tiny energy intervals) that were previously limited by the energy resolution of EELS can be detected in this work, benefiting from the advances in monochromators over the past decade. Moreover, STEM-EELS is also promising for probing the coherent interactions between electrons and resonating light fields for strong electron-light coupling and quantum optics of free electrons,[48,49] which is another exciting emerging field, e.g., investigation of the strong electron-photon coupling with a sufficient pump light field in the nanowire structures. Therefore, the advantages of this cutting-edge technique demonstrated in this work are expected to play an increasingly important role in multiple fields such as nano-optics, quantum optics, and nanoscience and -technology in the future.

In summary, the electron−photon interactions in individual SiC nanowires are investigated via STEM-EELS, and two types of optical cavity resonating modes, supported by the longitudinal FP resonating waveguide modes and the transverse WGMs, are simultaneously excited through inelastic electron scattering, which spans from ultraviolet to near-infrared spectra. The electron−photon interactions exhibit a much wider energy

https://doi.org/10.1021/acs.nanolett.2c01672
Nano Lett. 2022, 22, 6207−6214

and momentum match than photon−photon, thus the single nanowire cavity modes excited by electrons may exhibit potential applications in the design of nanoscale optoelectronic devices. Our work provides a new alternative technique to study the optical resonating spectroscopy of a single nanowire and to explore the light−matter interactions in dielectric nanostructures, which is also promising for modulating free electrons via photonic structures.

METHODS

EELS Data Acquisition. The EELS data were acquired on a Nion U-HERMES200 microscope equipped with both a monochromator and aberration correctors, with a 60 kV work voltage and a ∼20 pA beam current. The beam convergence semiangle of 20 mrad was used, while the collection semiangle was 25 mrad. The spot size of the electron beam is about 200 pm and scanned with the line positioned ∼10 nm away from the SiC nanowire edge.

Theoretical Modeling of Optical Modes in SiC Nanowire. Let us first consider the longitudinal propagating modes in an infinite cylindrical SiC nanowire with a radius of a. The electromagnetic fields in the nanowire are expressed in cylindrical coordinates as $\vec{E} = \vec{E}(\vec{r})e^{-i(\omega t-\beta z)}$, $\vec{H} = \vec{H}(\vec{r})e^{-i(\omega t-\beta z)}$, where ω is the angular frequency and β is the propagation constant. We can obtain two sets of wave equations derived from the Maxwell equations:

$$\begin{cases} \dfrac{\partial^2 E_z}{\partial r^2} + \dfrac{1\partial E_z}{r\partial r} + \dfrac{1\partial^2 E_z}{r^2\partial\theta^2} + [k_0^2\varepsilon(\vec{r}) - \beta^2]E_z = 0 \\ \dfrac{\partial^2 H_z}{\partial r^2} + \dfrac{1\partial H_z}{r\partial r} + \dfrac{1\partial^2 H_z}{r^2\partial\theta^2} + [k_0^2\varepsilon(\vec{r}) - \beta^2]H_z = 0 \end{cases} \quad (1)$$

where k_0 is the vacuum wave-vector, $\varepsilon(\vec{r})$ is the relative permittivity of the SiC nanowire and its surroundings, i.e., $\varepsilon(\vec{r}) = \varepsilon_1 = \varepsilon_{SiC}(\omega)$, $r \le a$, and $\varepsilon(\vec{r}) = \varepsilon_2 = 1$, $r > a$. Given the boundary condition that the tangential electric/magnetic field components should be continuous at the interface, and the fact that the field is convergent at $r = 0$ and $r = \infty$, we can obtain the eigen-equation for different waveguide modes:[34,50]

$$\left[\frac{J_n'(\mu)}{\mu J_n(\mu)} + \frac{K_n'(w)}{wK_n(w)}\right]\left[\frac{J_n'(\mu)}{\mu J_n(\mu)} + \frac{\varepsilon_2}{\varepsilon_1}\frac{K_n'(w)}{wK_n(w)}\right] = n^2\left(\frac{1}{\mu^2} + \frac{1}{w^2}\right)\left(\frac{1}{\mu^2} + \frac{\varepsilon_2}{\varepsilon_1}\frac{1}{w^2}\right) \quad (2)$$

where n is an integer (0, 1, 2, 3...), $J_n(x)$ is the nth-order Bessel function, $K_n(x)$ is modified Bessel functions of the second kind, and μ and w are defined as

$$\mu = a\sqrt{\varepsilon_1 k_0^2 - \beta^2},\ w = a\sqrt{\beta^2 - \varepsilon_2 k_0^2} \quad (3)$$

When $n = 0$, eq 2 is reduced to the following equations:

$$\begin{cases} \dfrac{J_0'(\mu)}{\mu J_0(\mu)} + \dfrac{K_0'(w)}{wK_0(w)} = 0, \text{ TE} \\ \dfrac{J_0'(\mu)}{\mu J_0(\mu)} + \dfrac{\varepsilon_2 K_0'(w)}{\varepsilon_1 wK_0(w)} = 0, \text{ TM} \end{cases} \quad (4)$$

The solutions to eq 4 generate the transverse electric TE (transverse magnetic TM) mode family, where the longitudinal electric field E_z (magnetic field H_z) is zero. When $n \neq 0$, the solution to eq 2 generates the HE and EH modes. The HE (EH) mode family indicates that the longitudinal electric (magnetic) field is relatively strong.

In eq 1, when $\beta = 0$, it indicates that the wave propagates totally in the transverse plane, which is also considered as WGM, and we have the following equations:

$$\begin{cases} \dfrac{\partial^2 E_z}{\partial r^2} + \dfrac{1\partial E_z}{r\partial r} + \dfrac{1\partial^2 E_z}{r^2\partial\theta^2} + k_0^2\varepsilon(\vec{r})E_z = 0 \\ \dfrac{\partial^2 H_z}{\partial r^2} + \dfrac{1\partial H_z}{r\partial r} + \dfrac{1\partial^2 H_z}{r^2\partial\theta^2} + k_0^2\varepsilon(\vec{r})H_z = 0 \end{cases} \quad (5)$$

The electromagnetic fields can be expressed as $\vec{E}(\vec{r})e^{-im\theta}$, and $\vec{H} = \vec{H}(\vec{r})e^{-im\theta}$, where m is an integer. Similarly, we can obtain the following eigen-equation by considering the boundary conditions:[51]

$$\left[\sqrt{\varepsilon_1}\frac{J_m(\sqrt{\varepsilon_1}k_0a)}{J_m'(\sqrt{\varepsilon_1}k_0a)} - \sqrt{\varepsilon_2}\frac{H_m^{(1)}(\sqrt{\varepsilon_2}k_0a)}{H_m'^{(1)}(\sqrt{\varepsilon_2}k_0a)}\right]\left[\sqrt{\varepsilon_2}\frac{J_m(\sqrt{\varepsilon_1}k_0a)}{J_m'(\sqrt{\varepsilon_1}k_0a)} - \sqrt{\varepsilon_1}\frac{H_m^{(1)}(\sqrt{\varepsilon_2}k_0a)}{H_m'^{(1)}(\sqrt{\varepsilon_2}k_0a)}\right] = 0 \quad (6)$$

where $H_m^{(1)}(x)$ is the Hankel function of the first kind. The solutions to eq 6 can be further divided into two groups, i.e., whispering-gallery TE (WTE) and whispering-gallery TM (WTM):

$$\begin{cases} \sqrt{\varepsilon_1}\dfrac{J_m'(\sqrt{\varepsilon_1}k_0a)}{J_m(\sqrt{\varepsilon_1}k_0a)} - \sqrt{\varepsilon_2}\dfrac{H_m'^{(1)}(\sqrt{\varepsilon_2}k_0a)}{H_m^{(1)}(\sqrt{\varepsilon_2}k_0a)} = 0, \text{ WTE} \\ \sqrt{\varepsilon_2}\dfrac{J_m'(\sqrt{\varepsilon_1}k_0a)}{J_m(\sqrt{\varepsilon_1}k_0a)} - \sqrt{\varepsilon_1}\dfrac{H_m'^{(1)}(\sqrt{\varepsilon_2}k_0a)}{H_m^{(1)}(\sqrt{\varepsilon_2}k_0a)} = 0, \text{ WTM} \end{cases} \quad (7)$$

Note that the WTE (WTM) polarization modes indicate that the electric field component (magnetic field component) is only E_z (H_z).

The interaction of electron beams and SiC nanowires can be treated as follows: the dipole radiation of a moving electron induced the polarization field of a photonic nanowire, which in turn acts on the electron and brings the energy loss. The generated electron energy loss can be expressed as[34,44]

$$\Gamma_{EELS}(\omega) = \frac{e^2}{\pi\hbar\omega}\iint \cos\left[\frac{\omega(z-z')}{v}\right] \times Im\left[\frac{E_z^{ind}(r, z, \omega)}{p_z(r', z', \omega)}\right]dz\,dz' \quad (8)$$

Here, we suppose the electron with a velocity of v moves along the z direction, and the electron is modeled as an electric dipole of amplitude $p_z(z,\omega)$. $E_z^{ind}(z,\omega)$ is the electron-induced electric field of the nanowire structure; $-e$ is the electron charge, $\hbar$ is the reduced Planck's constant, ω is the angular frequency. Under the mean field approximation, eq 8 can be rewritten as

$$\Gamma_{EELS}(\omega) \approx \frac{e^2}{\pi\hbar\omega}A \times Im\left[\frac{E_z^{ind}(r_0, z_0, \omega)}{p_z(r_0, z_0, \omega)}\right] \quad (9)$$

https://doi.org/10.1021/acs.nanolett.2c01672
Nano Lett. 2022, 22, 6207−6214

where A is the effective interaction area and r_0 is the average interaction distance. We expand the $E_z^{ind}(r_0,z_0,\omega)$ by the eigen-photonic mode of the nanowires and obtained $E_z^{ind}(r_0,z_0,\omega) = \alpha(\omega)\, E_z^{eigen}(r_0,z_0,\omega)$, where $\alpha(\omega)$ is the excited field amplitude and is calculated through the spatial overlap integral of the dipole field and a photonic-eigen mode:

$$\alpha(\omega) = \iint p(\vec{r}, z_0, \omega)\cdot E_z^{eigen,*}(\vec{r}, \omega)\, d\vec{r} \tag{10}$$

Note that $E_z^{eigen}(r_0,z_0,\omega)$ of a cylinder nanowire structure has analytical expressions as explicitly discussed in the first section. Finally, substituting these expressions into eq 9, we obtained the electron loss spectra as

$$\Gamma_{EELS}(\omega) = \frac{e^2}{\pi\hbar\omega} A \times Im\left[\frac{\alpha(\omega)E_z^{eigen}(r_0, z_0, \omega)}{p_z(r_0, z_0, \omega)}\right] \tag{11}$$

■ ASSOCIATED CONTENT

Supporting Information

The Supporting Information is available free of charge at https://pubs.acs.org/doi/10.1021/acs.nanolett.2c01672.

Structure of SiC, EELS measurements in another SiC nanowire with a length/diameter ratio of 22.5, and EELS profile at an energy of 1.5 eV along the SiC nanowire (PDF)

■ AUTHOR INFORMATION

Corresponding Authors

Yun-Feng Xiao − *State Key Laboratory for Mesoscopic Physics and Frontiers Science Center for Nano-optoelectronics, School of Physics, Peking University, Beijing 100871, China;* orcid.org/0000-0002-0296-7130; Email: yfxiao@pku.edu.cn

Peng Gao − *Electron Microscopy Laboratory, School of Physics, International Center for Quantum Materials, and Interdisciplinary Institute of Light-Element Quantum Materials and Research Center for Light-Element Advanced Materials, Peking University, Beijing 100871, China; Collaborative Innovation Center of Quantum Matter, Beijing 100871, China;* orcid.org/0000-0003-0860-5525; Email: p-gao@pku.edu.cn

Authors

Jinlong Du − *Electron Microscopy Laboratory, School of Physics, Peking University, Beijing 100871, China;* orcid.org/0000-0003-2776-0950

Jin-hui Chen − *State Key Laboratory for Mesoscopic Physics and Frontiers Science Center for Nano-optoelectronics, School of Physics, Peking University, Beijing 100871, China; Institute of Electromagnetics and Acoustics, Xiamen University, Xiamen 361005, China*

Yuehui Li − *Electron Microscopy Laboratory, School of Physics and International Center for Quantum Materials, Peking University, Beijing 100871, China*

Ruochen Shi − *Electron Microscopy Laboratory, School of Physics and International Center for Quantum Materials, Peking University, Beijing 100871, China*

Mei Wu − *Electron Microscopy Laboratory, School of Physics and International Center for Quantum Materials, Peking University, Beijing 100871, China*

Complete contact information is available at: https://pubs.acs.org/10.1021/acs.nanolett.2c01672

Author Contributions

[∇]These authors contributed equally. P.G. and Y.X. conceived the research. J.D., J.C., and Y.L. performed the main experiments and data analysis. M.W. performed experiments. J.D., J.C., Y.L., P.G., and Y.X. wrote the manuscript with inputs from all authors. The manuscript was written through contributions of all authors. All authors have given approval to the final version of the manuscript.

Notes

The authors declare no competing financial interest.

■ ACKNOWLEDGMENTS

This work was supported by the National Natural Science Foundation of China (Grant No. 12004010, 52125307, 11974023, U20B2025, 62005231). The authors acknowledge Electron Microscopy Laboratory of Peking University, China for the use of a Cs-corrected Nion U-HERMES200 scanning transmission electron microscope and financial support. We thank Prof. Qing Zhang and Prof. Dong Sun for assistance in data analysis and thank Dr. Chenglong Shi for assistance in microscope operation.

■ REFERENCES

(1) Basov, D. N.; Fogler, M. M.; Garcia de Abajo, F. J. Polaritons in van der Waals material. *Science* **2016**, *354*, aag1992.

(2) Li, N.; Guo, X.; Yang, X.; Qi, R.; Qiao, T.; Li, Y.; Shi, R.; Li, Y.; Liu, K.; Xu, Z.; Liu, L.; García de Abajo, F. J.; Dai, Q.; Wang, E.-G.; Gao, P. Direct observation of highly confined phonon polaritons in suspended monolayer hexagonal boron nitride. *Nat. Mater.* **2021**, *20*, 43−48.

(3) Zhu, X.; Shi, L.; Schmidt, M. S.; Boisen, A.; Hansen, O.; Zi, J.; Xiao, S.; Mortensen, N. A. Enhanced light−matter interactions in graphene-covered gold nanovoid arrays. *Nano Lett.* **2013**, *13*, 4690−4696.

(4) Zhang, J.; Tang, Y.; Lee, K.; Ouyang, M. Tailoring light−matter−spin interactions in colloidal hetero-nanostructures. *Nature* **2010**, *466*, 91−95.

(5) Dorfmüller, J.; Vogelgesang, R.; Weitz, R. T.; Rockstuhl, C.; Etrich, C.; Pertsch, T.; Lederer, F.; Kern, K. Fabry-Pérot resonances in one-dimensional plasmonic nanostructures. *Nano Lett.* **2009**, *9*, 2372−2377.

(6) Piazza, L.; Lummen, T. T.; Quinonez, E.; Murooka, Y.; Reed, B. W.; Barwick, B.; Carbone, F. Simultaneous observation of the quantization and the interference pattern of a plasmonic near-field. *Nat. Commun.* **2015**, *6*, 6407.

(7) McParland, B. J.*Nuclear Medicine Radiation Dosimetry: Advanced Theoretical Principles*; Springer London: London, 2010.

(8) Nozières, P.; Pines, D. Electron interaction in solids. characteristic energy loss spectrum. *Phys. Rev.* **1959**, *113*, 1254−1267.

(9) Losquin, A.; Kociak, M. Link between cathodoluminescence and electron energy loss spectroscopy and the radiative and full electromagnetic local density of states. *ACS Photonics* **2015**, *2*, 1619−1627.

(10) Dai, S.; Fei, Z.; Ma, Q.; Rodin, A. S.; Wagner, M.; McLeod, A. S.; Liu, M. K.; Gannett, W.; Regan, W.; Watanabe, K.; Taniguchi, T.; Thiemens, M.; Dominguez, G.; Neto, A. H. C.; Zettl, A.; Keilmann, F.; Jarillo-Herrero, P.; Fogler, M. M.; Basov, D. N. Tunable phonon polaritons in atomically thin van der waals crystals of boron nitride. *Science* **2014**, *343*, 1125−1129.

(11) Fei, Z.; Andreev, G. O.; Bao, W.; Zhang, L. M.; McLeod, A. S.; Wang, C.; Stewart, M. K.; Zhao, Z.; Dominguez, G.; Thiemens, M.; Fogler, M. M.; Tauber, M. J.; Castro-Neto, A. H.; Lau, C. N.; Keilmann, F.; Basov, D. N. Infrared nanoscopy of dirac plasmons at the graphene−SiO_2 interface. *Nano Lett.* **2011**, *11*, 4701−4705.

(12) Alfaro-Mozaz, F. J.; Alonso-González, P.; Vélez, S.; Dolado, I.; Autore, M.; Mastel, S.; Casanova, F.; Hueso, L. E.; Li, P.; Nikitin, A. Y.;

Hillenbrand, R. Nanoimaging of resonating hyperbolic polaritons in linear boron nitride antennas. *Nat. Commun.* **2017**, *8*, 15624.
(13) Qi, R.; Wang, R.; Li, Y.; Sun, Y.; Chen, S.; Han, B.; Li, N.; Zhang, Q.; Liu, X.; Yu, D.; Gao, P. Probing far-infrared surface phonon polaritons in semiconductor nanostructures at nanoscale. *Nano Lett.* **2019**, *19*, 5070−5076.
(14) Wei, H.; Pan, D.; Zhang, S.; Li, Z.; Li, Q.; Liu, N.; Wang, W.; Xu, H. Plasmon waveguiding in nanowires. *Chem. Rev.* **2018**, *118*, 2882−2926.
(15) Khatib, O.; Bechtel, H. A.; Martin, M. C.; Raschke, M. B.; Carr, G. L. Far infrared synchrotron near-field nanoimaging and nanospectroscopy. *ACS Photonics* **2018**, *5*, 2773−2779.
(16) Li, P.; Lewin, M.; Kretinin, A. V.; Caldwell, J. D.; Novoselov, K. S.; Taniguchi, T.; Watanabe, K.; Gaussmann, F.; Taubner, T. Hyperbolic phonon-polaritons in boron nitride for near-field optical imaging and focusing. *Nat. Commun.* **2015**, *6*, 7507.
(17) Atkin, J. M.; Raschke, M. B. Optical spectroscopy goes intramolecular. *Nature* **2013**, *498*, 44−45.
(18) Flack, F.; Samarth, N.; Nikitin, V.; Crowell, P. A.; Shi, J.; Levy, J.; Awschalom, D. D. Near-field optical spectroscopy of localized excitons in strained CdSe quantum dots. *Phys. Rev. B* **1996**, *54*, R17312−R17315.
(19) Francoeur, S.; Klem, J. F.; Mascarenhas, A. Optical spectroscopy of single impurity centers in semiconductors. *Phys. Rev. Lett.* **2004**, *93*, 067403.
(20) Xu, X. G.; Ghamsari, B. G.; Jiang, J.-H.; Gilburd, L.; Andreev, G. O.; Zhi, C.; Bando, Y.; Golberg, D.; Berini, P.; Walker, G. C. One-dimensional surface phonon polaritons in boron nitride nanotubes. *Nat. Commun.* **2014**, *5*, 4782.
(21) Keilmann, F.; Hillenbrand, R. Near-field microscopy by elastic light scattering from a tip. *Philos. Trans. R. Soc. London Ser. A-Math. Phys. Eng. Sci.* **2004**, *362*, 787−805.
(22) Raether, H. Surface-plasmons on smooth and rough surfaces and on gratings. *Springer Trac. Mod. Phys.* **1988**, *111*, 1−133.
(23) Polman, A.; Kociak, M.; Garcia de Abajo, F. J. Electron-beam spectroscopy for nanophotonics. *Nat. Mater.* **2019**, *18*, 1158−1171.
(24) Krivanek, O. L.; Lovejoy, T. C.; Dellby, N.; Aoki, T.; Carpenter, R. W.; Rez, P.; Soignard, E.; Zhu, J.; Batson, P. E.; Lagos, M. J.; Egerton, R. F.; Crozier, P. A. Vibrational spectroscopy in the electron microscope. *Nature* **2014**, *514*, 209−212.
(25) Krivanek, O. L.; Lovejoy, T. C.; Murfitt, M. F.; Skone, G.; Batson, P. E.; Dellby, N.*Electron Microscopy and Analysis Group Conference 2013*; Journal of Physics: Conference Series; IOP Publishing, 2014.
(26) Dwyer, C.; Aoki, T.; Rez, P.; Chang, S. L. Y.; Lovejoy, T. C.; Krivanek, O. L. Electron-beam mapping of vibrational modes with nanometer spatial resolution. *Phys. Rev. Lett.* **2016**, *117*, 256101.
(27) Lagos, M. J.; Trugler, A.; Hohenester, U.; Batson, P. E. Mapping vibrational surface and bulk modes in a single nanocube. *Nature* **2017**, *543*, 529−532.
(28) Hage, F. S.; Kepaptsoglou, D. M.; Ramasse, Q. M.; Allen, L. J. Phonon spectroscopy at atomic resolution. *Phys. Rev. Lett.* **2019**, *122*, 016103.
(29) Hage, F. S.; Radtke, G.; Kepaptsoglou, D. M.; Lazzeri, M.; Ramasse, Q. M. Single-atom vibrational spectroscopy in the scanning transmission electron microscope. *Science* **2020**, *367*, 1124−1127.
(30) Hage, F. S.; Ramasse, Q. M.; Allen, L. J. Contrast reversal in atomic-scale phonon spectroscopic imaging. *Phys. Rev. B* **2020**, *102*, 214111.
(31) Li, Y.; Qi, R.; Shi, R.; Li, N.; Gao, P. Manipulation of surface phonon polaritons in SiC nanorods. *Sci. Bull.* **2020**, *65*, 820−826.
(32) Li, Y. H.; Wu, M.; Qi, R. S.; Li, N.; Sun, Y. W.; Shi, C. L.; Zhu, X. T.; Guo, J. D.; Yu, D. P.; Gao, P. Probing lattice vibrations at SiO_2/Si surface and interface with nanometer resolution. *Chin. Phys. Lett.* **2019**, *36*, 026801.
(33) Qi, R.; Shi, R.; Li, Y.; Sun, Y.; Wu, M.; Li, N.; Du, J.; Liu, K.; Chen, C.; Chen, J.; Wang, F.; Yu, D.; Wang, E.-G.; Gao, P. Measuring phonon dispersion at an interface. *Nature* **2021**, *599*, 399−403.
(34) García de Abajo, F. J. Optical excitations in electron microscopy. *Rev. Mod. Phys.* **2010**, *82*, 209−275.
(35) Talebi, N. Interaction of electron beams with optical nanostructures and metamaterials: from coherent photon sources towards shaping the wave function. *J. Opt.* **2017**, *19*, 103001.
(36) Kfir, O. Entanglements of electrons and cavity photons in the strong-coupling regime. *Phys. Rev. Lett.* **2019**, *123*, 103602.
(37) Huang, S. Y.; Shi, R. C.; Li, Y. H.; Wu, M.; Li, N.; Du, J. L.; Yu, D. P.; Gao, P. Recent progress of vibrational electron energy-loss spectroscopy in scanning transmission electron microscope. *Chin. J. Vac. Sci. Technol.* **2021**, *41*, 213−224.
(38) Lourenço-Martins, H.; Kociak, M. Vibrational surface electron-energy-loss spectroscopy probes confined surface-phonon modes. *Phys. Rev. X* **2017**, *7*, 041059.
(39) Liu, B.; Li, N.; Sun, Y.; Li, Y.; Gao, P.; Yu, D. Nanoscale measurement of surface phonon via STEM-EELS. *J. Chin. Electron Microsc. Society* **2019**, *37*, 474−480.
(40) Poursoti, Z.; Sun, W.; Bharadwaj, S.; Malac, M.; Iyer, S.; Khosravi, F.; Cui, K.; Qi, L.; Nazemifard, N.; Jagannath, R.; Rahman, R.; Jacob, Z. Deep ultra-violet plasmonics: exploiting momentum-resolved electron energy loss spectroscopy to probe germanium. *Opt. Express* **2022**, *30*, 12630−12638.
(41) Wang, C.; Fang, Z.; Yi, A.; Yang, B.; Wang, Z.; Zhou, L.; Shen, C.; Zhu, Y.; Zhou, Y.; Bao, R.; Li, Z.; Chen, Y.; Huang, K.; Zhang, J.; Cheng, Y.; Ou, X. High-Q microresonators on 4H-silicon-carbide-on-insulator platform for nonlinear photonics. *Light-Sci. Appl.* **2021**, *10*, 139.
(42) Wang, Y.; Lin, Q.; Feng, P. X. L. Single-crystal 3C-SiC-on-insulator platform for integrated quantum photonics. *Opt. Express* **2021**, *29*, 1011−1022.
(43) Adolph, B.; Tenelsen, K.; Gavrilenko, V. I.; Bechstedt, F. Optical and loss spectra of SiC polytypes from ab initio calculations. *Phys. Rev. B* **1997**, *55*, 1422−1429.
(44) Cao, Y.; Manjavacas, A.; Large, N.; Nordlander, P. Electron Energy-Loss Spectroscopy Calculation in Finite-Difference Time-Domain Package. *ACS Photonics* **2015**, *2*, 369−375.
(45) Yan, R.; Gargas, D.; Yang, P. Nanowire photonics. *Nat. Photonics* **2009**, *3*, 569−576.
(46) Eaton, S. W.; Fu, A.; Wong, A. B.; Ning, C.-Z.; Yang, P. Semiconductor nanowire lasers. *Nat. Rev. Mater.* **2016**, *1*, 16028.
(47) Pongruengkiat, W.; Pechprasarn, S. Whispering-Gallery Mode Resonators for Detecting Cancer. *Sensors-Basel* **2017**, *17*, 2095.
(48) Kfir, O.; Lourenco-Martins, H.; Storeck, G.; Sivis, M.; Harvey, T. R.; Kippenberg, T. J.; Feist, A.; Ropers, C. Controlling free electrons with optical whispering-gallery modes. *Nature* **2020**, *582*, 46−49.
(49) Wang, K. P.; Dahan, R.; Shentcis, M.; Kauffmann, Y.; Ben Hayun, A.; Reinhardt, O.; Tsesses, S.; Kaminer, I. Coherent interaction between free electrons and a photonic cavity. *Nature* **2020**, *582*, 50−54.
(50) Okamoto, K.*Fundamentals of Optical Waveguides*; Academic Press: Burlington, 2006.
(51) Heebner, J.; Grover, R.; Ibrahim, T. A.*Optical Microresonators*; Springer Series in Optical Sciences: New York, 2008.

https://doi.org/10.1021/acs.nanolett.2c01672
Nano Lett. 2022, 22, 6207−6214